# Compact Continuous Wave Radar for Water Level Monitoring

SHANYUE GUAN,[a] JENNIFER A. BRIDGE,[b] JUSTIN R. DAVIS,[b] AND CHANGZHI LI[c]

[a] *Department of Engineering, East Carolina University, Greenville, North Carolina*
[b] *Department of Civil and Coastal Engineering, University of Florida, Gainesville, Florida*
[c] *Department of Electrical and Computer Engineering, Texas Tech University, Lubbock, Texas*

(Manuscript received 7 May 2021, in final form 7 February 2022)

ABSTRACT: There is a demand for noncontact, high-accuracy, high-spatial-resolution, wireless sensing technologies for various water level and coastal monitoring applications. This paper presents a low-cost, compact, easily configurable interferometry radar for noncontact water level monitoring, including its hardware design, signal processing algorithms, and wireless communication strategies. Interferometry radar measures distance by comparing the phase lag between reflected and transmitted signals. Water level measurements using this approach have been demonstrated in a solitary wave laboratory experiment, a field deployment observing wave run-up near Ponte Vedra, Florida, and a field deployment observing waves and tides in the Sparkill Creek located in Piermont, New York. The experimental results from the radars with millimeter-level accuracy have been compared with reference sensors and demonstrate the potential of continuous wave radar for water level observations.

KEYWORDS: Ocean; In situ oceanic observations; Instrumentation/sensors; Measurements; Microwave observations; Radars/Radar observations

## 1. Introduction

Water level data are often used to track and model long- and short-term coastal processes (Grabemann and Weisse 2008; Poate et al. 2013). Long-term processes such as sea level rise, beach erosion, sediment transport, and hydrological sustainability are affected by the coastal water levels and waves. Monitoring water levels over a long period and large area is critical to accurately model and predict these slow-changing processes (Nerem et al. 2010). Tracking the water level near shorelines is important to estimate beach erosion rates (Theuerkauf et al. 2014), while swash zone run-up and wetland water elevation monitoring enables the characterization of sediment transport and hydrological sustainability (Warner et al. 2008). In addition to long-term wave processes, short-term, extreme events such as wind-driven storm surge, have damaging effects on coastal infrastructure and public safety (Möller et al. 2014; Wahl et al. 2015; Pistrika and Jonkman 2010). Monitoring the rapid changes of water levels in real-time high sampling rates adequate to capture both wave and mean water level signals provides data to inform emergency response and assess postevent infrastructure conditions. The ability to accurately measure long- and short-term coastal wave processes with high spatial and temporal resolution using low-cost measurement techniques has the potential to improve coastal process tracking and modeling as well as real-time assessment for decision support.

This paper presents a low-cost, noncontact water level sensor based on portable radar interferometry that can be used to provide accurate, real-time, high-spatial-resolution measurements. The radar is installed in a known position above the water to provide continuous measurement of the distance between the radar antennas and the water surface. Our approach provides a continuous measurement of the distance between the radar antennas and the water surface. A module generating 2.4 GHz RF signals is integrated with a microcontroller and wireless communication device that transmits the observations in real time. Multiple radars may operate in a network to provide synchronized measurements in a region of interest and the sampling rate of the sensor may be configured to capture relatively low frequency (<~1 Hz: seiches, tides, etc.), medium frequency (~1–10 Hz: wind driven waves/swell, run-up, etc.) or high frequency (>~10 Hz: capillary waves, antenna vibration, etc.) signals. The radar system described in this paper is specifically designed for low- and medium-frequency measurements. The radar's theory of operation, hardware design, and signal processing used to extract water level observations are presented. This novel technology was recently awarded a patent (U.S. 10 436 625 B2) and has been deployed to measure water level in both laboratory and field environments, including controlled wave flume tests, field measurement of beach run-up and waves/flood levels in a tidally influenced creek. The water level measurement performance of the radar is summarized.

## 2. Water level measurement technologies

Water level sensors can be divided into two major types based on their operating principles: contact and noncontact measurement sensors. Some contact sensors are installed at a fixed location either fully or partially submerged in the water. Resistive or capacitive water level gauges are examples of fixed sensors and have very high resolution and sensitivity to water level changes (Anderson et al. 1972; Aravamudhan and Bhansali 2008; Arnaud et al. 2009; Ferreira et al. 2012); however, these sensors are subject to nonlinearity errors (Bera et al. 2006). Other types of contact measurement sensors are installed at the water surface, usually attached to a floating

*Corresponding author*: Shanyue Guan, guans18@ecu.edu

DOI: 10.1175/JTECH-D-21-0059.1

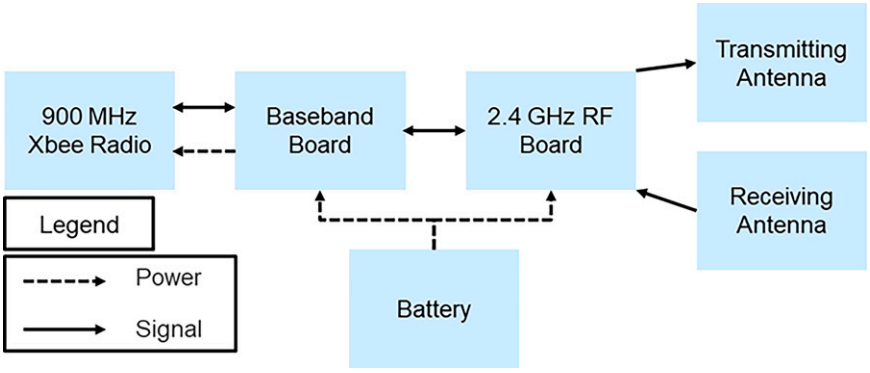


FIG. 1. Diagram of the continuous wave radar major components (version 1 system integrated microprocessor with baseband board, generation 2 microprocessor installed separately).

device, and their positions vary with the water surface. These floating sensors can provide high-accuracy water level measurements (Goodman and Levine 1990; Oroza et al. 2013; Yang et al. 2007), but the large size and high cost limit their applications for large-area monitoring (Farooqui et al. 2014). GPS has been applied to measure water level over large areas by installing the GPS receivers on floating buoys (Kelecy et al. 1994; Larson et al. 2013; Wöppelmann et al. 2007); however, GPS suffers from large systematic error in the vertical direction, making it difficult to achieve the wave level measurement with a reasonable accuracy. Additionally, a challenge with contact sensors is the ever-present threat of biofouling, which decreases signal to noise ratios and increases maintenance costs and efforts.

Noncontact sensors avoid many implementation challenges of contact measurement approaches and can measure water levels from a few meters to several kilometers away (Jeswin et al. 2017; Kraus et al. 1994; Rorbaek and Andersen 2000; Turner et al. 2008). For example, ultrasonic sensors measure the water elevation from a few meters above the surface; however, the speed of sound is affected by temperature, requiring sophisticated temperature compensation to achieve accurate measurements (Fisher and Sui 2013). Pulse radar–based technology has been explored for water level measurement applications (Barjenbruch et al. 2002; Park et al. 2014). Most existing radar technologies suffer from the mixing of the radio signal backscattered from the different boundaries and from the background noise (Barjenbruch et al. 2002). K-band radars have also been used for water observations (Cui et al. 2018, 2019). Remote sensing approaches, such as airborne lidar (Gesch 2009; Poulter and Halpin 2008; Zhang 2011) or satellite imagery (Collard et al. 2005; D'Asaro et al. 2014; Izaguirre et al. 2011; Krogstad and Barstow 1999) are capable of measuring a mean water level over large areas, but cannot provide high-resolution measurement at specific locations of interest.

In addition to these drawbacks, many existing sensors do not sample at adequate rates to monitor rapid water level changes caused by surface waves. To better monitor the water level for both long- and short-term processes, this paper presents a low-cost, high-sampling-rate sensor based on continuous wave radar technology.

## 3. Continuous wave radar design

Continuous wave (CW) radar provides noncontact measurement of the distance between a set of radar antenna and a target. Via one antenna, CW radar transmits a continuous microwave at a constant carrier frequency. The transmitted signal is reflected by the target and received by the second antenna. After processing the received signal, the distance between the target and the antennas can be obtained. CW radar has been validated successfully to measure structural displacement (Guan et al. 2018, 2017, 2015; Pieraccini et al. 2004) and human chest wall motion (Li and Lin 2008; Li et al. 2013). When an appropriate wavelength of the radar carrier wave is used, the surface water can provide a strong reflection of the microwave signal. Assuming the CW radar has a stationary location and/or its movement is known, water level can be determined from the time-varying phase shift between transmitted and received signals. The CW radar measurement approach provides a continuous measurement of the distance between the radar antennas and the water surface. As a result, in terms of absolute distance, any nonwave contributions to motions of the antennas (e.g., vibration) or water surface (e.g., currents, atmospheric pressure changes) would also be captured in a manner similar to other timing-based, pulsed-signal related technologies (e.g., laser, acoustic, radar). For an antenna mounted perpendicularly above the water, horizontal currents would not impart any additional Doppler effect as the direction of the current is neither toward nor away from the antenna.

### a. *Continuous wave radar hardware design*

Two generations of CW radar sensors were designed for water level monitoring applications and are presented in this paper. Both sensor generations consist of the five major components shown in Fig. 1: 1) a matched pair of patch antennas for transmitting and receiving radar signals, 2) a radio frequency (RF) board that generates the radar signals, 3) a baseband board which down converts the raw radar signals to baseband signals and performs DC offset tuning with a microprocessor, 4) an XBee radio using Zigbee protocol, and 5) a power supply (DC batteries). The first-generation sensor has the microprocessor integrated onto the baseband board,

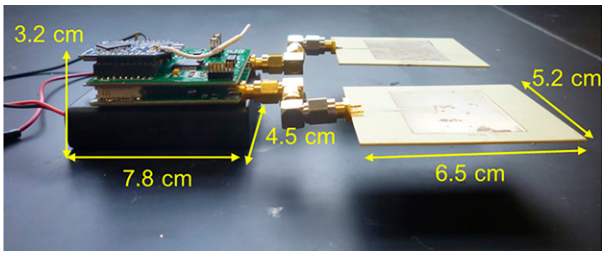


FIG. 2. First-generation continuous wave radar designed for structural vibration monitoring and adapted for water level monitoring.

while the second-generation sensor has a separate board for the microprocessor.

For water level monitoring, a 2.4 GHz (first-generation) or 5.8 GHz (second-generation) carrier frequency is selected to balance the hardware fabrication complexity, power consumption, and required signal strength. Both carrier frequencies have high reflectivity with the water surface. The beamwidth angle of the antennas is 45°; the resulting measurement is taken over an area on the target surface with a size proportional to the distance between the radar and the surface. The radar antenna and RF transmission power for the systems presented in this paper perform best when the radar's antenna is 1–2 m from the water surface. At these distances, our laboratory studies show good accuracy in the measured motion, especially for the wavelengths/period of interest. The design presented in this paper sought to balance antenna fabrication cost, antenna size, and power consumption with measurement effectiveness for the wave phenomena of interest; transmission power and antennas design can be adjusted for different measurement applications. The continuous microwave is generated by a voltage-controlled oscillator (VCO) on the RF board and transmitted by one of the antennas. The Doppler-shifted signal is reflected from the water surface and captured by the other antenna. The transmitted and received signals are combined by a mixer on the RF board and the resulting signal is transferred to the baseband board. The mixed signals are down converted to the baseband ($I$/$Q$) channels, which contain the water level information, on the baseband board. A low-power MSP43X microprocessor controls all system operations.

Although observed signals can be transmitted from the sensor by a variety of methods (cellular, 5 GHz Wi-Fi, Ethernet, etc.), for the applications described herein the baseband signals are communicated using Zigbee protocol with low-power, 900 MHz XBee radio modules. The 900 MHz XBee modules are used to avoid interference with the 2.4 GHz microwave signal generated by the first-generation radar. One XBee module is integrated with the baseband board of the radar and the other module is connected to a computer via USB as a data collection base station. Multiple CW radars may establish a wireless network via the Zigbee or LoRa protocol to monitor the water level information over a large area.

The required voltage range for the assembled radar system is 4.8–5.5 V, which is provided by batteries. Based on experimental results, using four 900 mAh AAA batteries, the radar can operate continuously for more than an hour; the use of larger batteries and/or intermittent operation and sleep cycling (e.g., Jang et al. 2010) results in much longer (weeks) operating time. The assembled components of the first-generation radar are shown in Fig. 2. Additional variations in the details of the hardware components and configuration between the system generations are described in section 3d.

### b. *Radar network wireless communication*

XBee radios on the radar(s) are configured to communicate with a single XBee radio located at the base station computer. The base station XBee radio is configured to allow communication with multiple radars simultaneously to support high-spatial-resolution sampling. To operate multiple radars simultaneously, transmitted bytes representing different radars, $I$/$Q$ signals, etc. must be uniquely differentiable from other bytes. To achieve this, a byte packing algorithm was developed to support one, two, or four radars transmitting data simultaneously (Table 1). Depending on

TABLE 1. The four supported radar configurations. The third and fourth configurations support four radars in either a low or high ADC resolution, respectively.

| No. of radars | ADC bits per $I$/$Q$ | Bytes per $I$/$Q$ | Total bytes | Bits for sequential $I$/$Q$ sections a–d (L = low bits; H = high bits) | Bits for radar No. ($N$) | Bits for $I$/$Q$ ($C$) | Bits for section ($S$) | Bits for ADC ($A$) |
|---|---|---|---|---|---|---|---|---|
| 1 | 12 | 2 | 4 | a: SCAAAAAA (L)<br>b: SCAAAAAA (H) | 0 | 1 | 1 | 6 |
| 2 | 10 | 2 | 8 | a: NCSAAAAA (L)<br>b: NCSAAAAA (H) | 1 | 1 | 1 | 5 |
| 4 (low) | 9 | 3 | 24 | a: NNCSSAAA (L)<br>b: NNCSSAAA<br>c: NNCSSAAA (H) | 2 | 1 | 2 | 3 |
| 4 (high) | 12 | 4 | 32 | a: NNCSSAAA (L)<br>b: NNCSSAAA<br>c: NNCSSAAA<br>d: NNCSSAAA (H) | 2 | 1 | 2 | 3 |

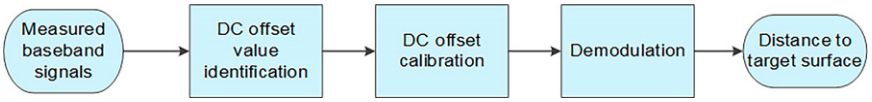


FIG. 3. Major signal processing steps from measured radar baseband signals to achieving distance to target surface.

the number of radars configured to operate simultaneously, between 4 (one radar, 12-bit accurate $I$ and $Q$) and 32 (four radars, 12-bit accurate $I$ and $Q$) bytes are required for a single water level observation. Specifically for the four-radar case, two ADCs (9 and 12 bits) are provided for different measurement resolution requirements. To reduce retransmissions, the XBee radios are typically setup with a baud rate of 38 400 to provide a good balance between communication reliability and bandwidth. This results in a usable water level sampling rate between 16 and 128 Hz, depending on the number of radars, the influence of the local RF environment, and the distance between the XBee modules.

### c. *Continuous wave radar signal processing*

The baseband ($I$/$Q$) signals generated by the radar are

$$B_I(t) = A_I \cos[\theta + 4\pi x(t)/\lambda + \Delta\varphi] + \mathrm{DC}_I, \quad (1)$$

$$B_Q(t) = A_Q \sin[\theta + 4\pi x(t)/\lambda + \Delta\varphi] + \mathrm{DC}_Q, \quad (2)$$

where $A_\mathrm{I}$ and $A_\mathrm{Q}$ are the amplitudes of $I$ and $Q$ signals, $\theta$ is a constant phase shift due to the transmission path and target surface, $\Delta\varphi$ is the total residual phase noise of the baseband signals, and $\mathrm{DC}_I$ and $\mathrm{DC}_Q$ are the DC offsets in $I$ and $Q$ baseband signals, respectively. The $4\pi x(t)/\lambda$ term is the phase information corresponding to the time-varying distance between the radar and the target, $x(t)$, and $\lambda$ is the carrier wavelength. For the applications presented in this paper, the target surface refers to the water surface.

Figure 3 summarizes the data processing steps required to convert the acquired baseband signals to water level information. These steps may be conducted on the PC after it receives the baseband data from the sensors, or the signal processing algorithms may be implemented on the sensor's microprocessor, resulting in the transmission of water elevation information to the PC.

The first step is to determine optimal DC offset values for use in DC offset calibration. Using DC offset values associated with the highest signal-to-noise-ratio (SNR) of the baseband signals ensures the highest water level measurement accuracy. A low-pass analog filter is applied to the raw baseband signals to minimize high frequency noise and increase the SNR. The data are then segmented and the SNR of each segment of the data is calculated. Segments meeting the threshold value of SNR (~26 dB) are selected to identify the DC offset values for the whole data record (Guan et al. 2014).

The primary source of DC offset is the reflected signal from stationary target(s) in the environment. This part of the DC offset can be cancelled by using a DC offset calibration algorithm to correct the baseband data. This is accomplished by subtracting the DC offset values and then scaling $I$/$Q$ signals by the amplitude values of the baseband $I$/$Q$ signals. Additional detail on DC offset calibration, including selecting the most appropriate method based on measurement conditions, is provided in Guan et al. (2014).

After calibrating the DC offsets of the baseband signals, the phase information associated with water level is determined through phase demodulation. There are three approaches to demodulate the phase: 1) arctangent demodulation, 2) arctangent demodulation with phase unwrapping, and 3) the differentiate and cross-multiply (DACM) method (Wang et al. 2014). The wavelength of the radar signals and the amplitude of the water level changes determine whether arctangent demodulation without phase unwrapping can be applied. When the water level changes are smaller than the wavelength (e.g., 12.5 cm for the 2.4 GHz carrier frequency), the water level measurement is determined through two-argument arctangent demodulation by

$$\psi(t) = \arctan[B_{Q,\mathrm{corr}}(t)/B_{I,\mathrm{corr}}(t)] = \theta + 4\pi x(t)/\lambda + \Delta\varphi, \quad (3)$$

$$\varphi(t) = 4\pi x(t)/\lambda, \quad (4)$$

where $B_{Q,\mathrm{corr}}(\mathrm{t})$ and $B_{I,\mathrm{corr}}(\mathrm{t})$ are baseband signals with DC offset cancelled, $\varphi(t)$ is proportional to the distance to the water surface, $x(t)$. The changes in the distance to the water surface can be obtained as $x(t) = x_0 + \varphi(t)\lambda/4\pi$, where $x_0$ is the initial distance to the water surface.

However, when the trajectory of baseband signals crosses the boundary between the first and the fourth quadrants in the constellation plot of the raw baseband signals as shown in Fig. 4, $\varphi(t)$ of the trajectory from Eq. (4), is out of the range $[-\pi, \pi]$, the range required for applying arctangent demodulation. In this case either "unwrapping" can be applied prior to arctangent demodulation or DACM can be used to remove the DC offset.

When applying arctangent demodulation with unwrapping, the first step is to check the phase angle information of the radar signals. If the phase is out of the range $[-\pi, \pi]$, then demodulation is performed only for the data within the range. For the data out of this range, the phase angle is shifted to the range $[-\pi, \pi]$ and demodulation is performed. The final step is to assemble all the demodulated results to obtain the correct water level measurement results.

Different from the first two methods, DACM demodulation calculates the forward differential values of each channel to calculate the water level. The discrete signal expression of DACM is as follows:

$$\varphi[n] = \sum_{k=2}^{n} \frac{I[k]\{Q[k] - Q[k-1]\} - \{I[k] - I[k-1]\}Q[k]}{I[k]^2 + Q[k]^2}. \quad (5)$$

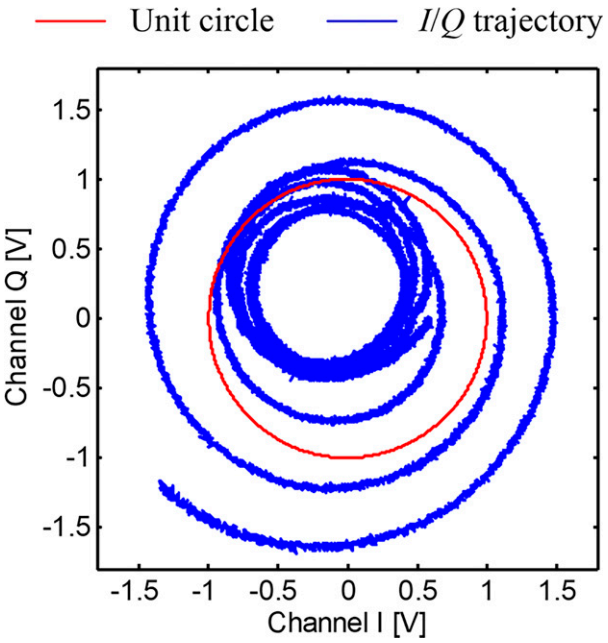


FIG. 4. Trajectories of baseband signals.

Since the DACM method does not use the arctangent function, it does not require phase unwrapping. However, the DACM method requires a higher level of computation compared with the arctangent method with unwrapping method due to its algorithm $O(N^2)$ complexity; this computational burden may not be appropriate when signal processing is carried out on the sensor microprocessor and power resources may be limited. Arctangent demodulation (with/without unwrapping) and DACM method demonstrate similar accuracy when analyzing the same set of data (Guan et al. 2014).

*d. Radar system versions and operating modes*

The two radar system generations are the result of the needs of the measurement applications and the technology available at the time of deployment. The first-generation system only supports saving data on a local base station computer and requires user input to operate and save data. The second generation has additional functionality that enables collected data to be sent to a remote home base computer and thus allows both interactive operation and autonomous, unattended operation. The following paragraphs provide detail on the differences between the two system versions and their modes of operation, which are summarized in Table 2.

The first-generation radar system consists of one or more radars installed at their measurement locations and a base station computer operated on-site within the transmission range of the radar's XBee radios. The system uses the MSP430 microprocessor integrated with baseband board to control all the operations (Gu et al. 2014). All operations are programmed using C and embedded on the microprocessor. The radars are housed in water resistant enclosures large enough to accommodate the sensor hardware and four D-cell alkaline batteries. The interior of the enclosure is filled with waterproof rubber and small openings are sealed with silicone to prevent any leakage. A water-resistant switch on the enclosure exterior controls the power status of the sensor. The base station computer uses a National Instruments LabView VI. All test parameters (such as the sampling rate) are set in LabView, which enables the initiation, visualization, storage, and termination of data collection. Although the radars automatically start streaming data to the computer via the XBee when turned on, system control on the base station computer is started manually, and data are only saved locally on the base station computer. This system version is useful for short-term, on-site tests.

The second-generation radar sensor system uses a larger weatherproof NEMA-4 rated enclosure for all sensor components and two eight C-cell battery packs to support longer unattended operation. The system uses the MSP432 Launchpad Microcontroller (MCU) with a Wi-Fi daughter board and an independent RF board. The embedded code on the MCU was developed using Energia and was designed for both operation of the radar and remote configuration via the XBee radio. At the receiving end, a Python script facilitates setting of data collection parameters and saving of data in a similar manner as the first-generation system. Instead of an external power switch, the system uses a float switch that turns the device on or off when the water level reaches a preset value, thus efficiently limiting power consumption to more significant episodic data collection. To avoid switch bouncing effects, the system is only powered off after the water stays below the trigger point for over a minute. The radar transmits data locally via the 900 MHz XBee to a main powered Linux base station computer running RHEL 7, which in turn sends data to a home location via cellular network. Data collected by the radar are first processed by Python scripts which injects the JSON-formatted observations into a Mosquitto MQTT telemetry server. At the base station, a databasing Python script the data in MQTT into a MongoDB NoSQL database while MQTT itself relays the data back to the home laboratory at the University of Florida (UF). At UF, MQTT makes the

TABLE 2. CW radar system generations and operating modes.

| Radar system version | Operation modes | Data collection | Software interface | Microprocessor and integration | Enclosure size/ batteries |
|---|---|---|---|---|---|
| Generation 1 | Interactive only | Continuous | LabView | MSP430 on baseband board | Small/4D cell |
| Generation 2 | Interactive or autonomous | Event driven | Python | MSP432 on separate board | Large/2 × 8C cell |

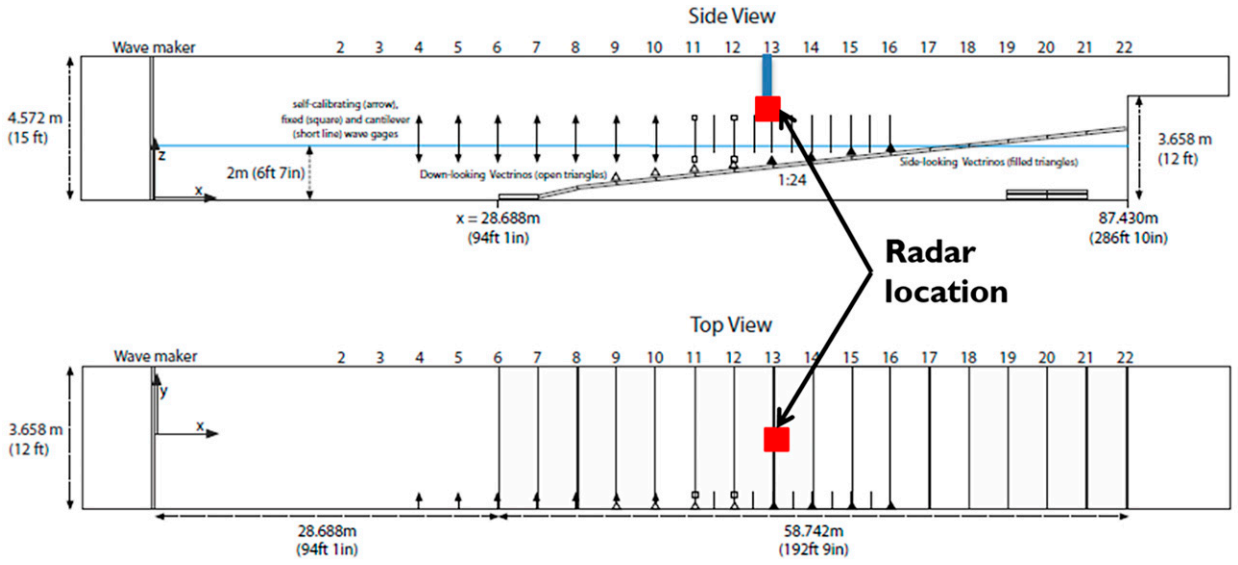


FIG. 5. Schematic of the wave tank with dimensions of 87.43 m × 3.658 m × 4.572 m (length × width × height).

data available for real-time viewing via a web service and another instance of the databasing script saves the data into another database for long-term archival. The entire system is designed for automated operation from end to end making it well suited to autonomously capture episodic, high water events at remote locations.

## 4. Water level monitoring experiments

To demonstrate the CW radar's ability to accurately observe water levels, a series of experimental tests were conducted under both laboratory and field conditions. Initial validation experiments were conducted at the O. H. Hinsdale Wave Research Laboratory at Oregon State University and were designed to test the radar's capabilities with pristine, undisturbed conditions (except for the signal) and compare the radar's performance to reference-quality wave gauges. In the first of three field tests, the radar observed the difficult-to-measure thickness of wave run-up in the swash zone at Mickler Beach, Florida. A second field test in Crescent Beach, Florida, used two radars operating in a network simultaneously to provide spatially distributed run-up measurements. In the final field test, a radar sensor was collocated with a pressure sensor in the Sparkill Creek along the Hudson River in Piermont, New York, with the intent of observing flooding events in the river with caused by storm surge, wind setup, or astronomically high tide events. The first-generation system was used for the laboratory experiments and the tests conducted at Mickler Beach and Crescent Beach with interactive mode; the second-generation system was deployed at Sparkill Creek in the autonomous operation mode.

### *a. Solitary wave detection*

To investigate the accuracy of the CW radar's water level measurement (wave height in this case), a series of tests with reference sensors were conducted in the Large Wave Flume at the O. H. Hinsdale Wave Research Laboratory at Oregon State University with the wave flume as shown in Fig. 5. The wave generator at one end of the wave flume generates user-specified waves with varying height, speed, and period. For the results presented herein, solitary waves with a 10-s period were used. The waves in the first test had a height of 10 cm and the second test had a height of 20 cm. To measure the wave height, the radar was mounted from the middle of a short span bridge over the wave tank with the radar's antennas facing toward the water surface. The mean height between the radar's antennas and the stationary water surface was 2 m. The distance between the radar's location and the wave generator was ~50 m. The wave gauges used as a comparison with the radar are located the same distance from the wave generator and mounted on the interior wall of the tank and submerged in the water. The wave gauge was a surface-

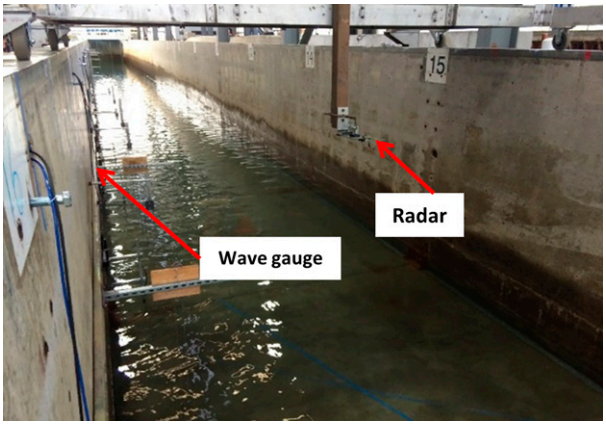


FIG. 6. Experimental setup.

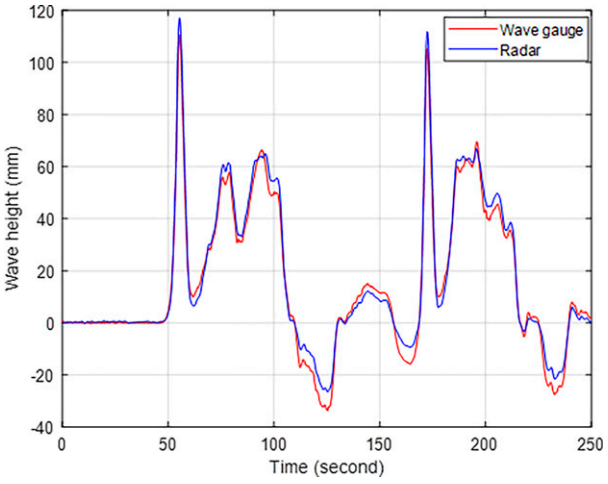


FIG. 7. Measurement results (10 cm solitary wave) from the wave gauge and radar sensor.

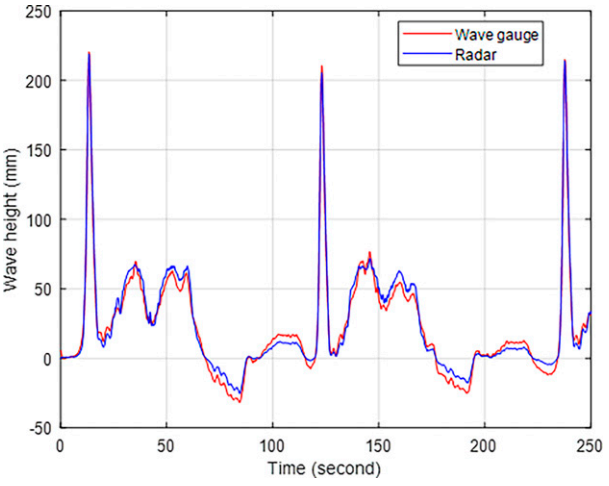


FIG. 8. Measurement results (20 cm solitary wave) from the wave gauge and radar sensor.

piercing resistance-type paired-wire gauge which can measure the wave height changes to submillimeter accuracy. The experimental setup is shown in Fig. 6. Data were collected during each series of waves with the radar sampled at 10 Hz. The radar's measurement was transmitted to the base station computer wirelessly via the XBee radio.

Arctangent demodulation with phase unwrapping was used for DC offset calibration in the processing of the baseband signals from these experiments. Figures 7 and 8 show the comparison between the radar and wave gauge measurements for the 10 and 20 cm waves, respectively. Noise from both radar and wave gauge measurements was reduced by applying the same low-pass filter with a cutoff frequency of 0.5 Hz. The figures show that the radar successfully measured the passage of the wave at the measurement location with good agreement to the wage gauge measurements. For Figs. 7 and 8, the maximum wave height differences between the radar and wave gauge measurements were 11.23 and 15.5 mm, respectively. Root-mean-square (RMS) of wave height measurements difference between the radar and wave gauges were 4.49 and 8.84 mm, respectively. The source of difference between the measurements may be the result of how and where each sensor operates. The radar measurements were taken over an area proportional to the height above the water; with a radar beam angle of 45° and a mean height above water of 2 m, the average measurement area diameter was 1.66 m centered over the tank. This area measurement had the effect of reducing the peaks in the water level observations. The wave gauge provided a point measurement of the height of the water at the interior wall. Although there were some differences from the measurement results, this experiment demonstrates that the radar sensor can detect water level changes within 10 mm accuracy.

### b. *Swash zone free surface elevation*

A series of tests were conducted at Mickler Beach, in Ponte Vedra, Florida, to determine the applicability of the radar for run-up measurements. The first-generation radar system was mounted on a support post driven into the sand to enable a freestanding measurement. The antennas of the radar were positioned 1 m above the initial sand surface as illustrated in Fig. 9. The radar was set to sample at 20 Hz, operating and measuring the water level for 15 min continuously. The data collected were sent to the base station computer which was set up ~15 m away from the sensor's location. The raw baseband signals from the radar are shown in Fig. 10. The wave information was retrieved from the baseband signals by conducting post signal processing in MATLAB. The obtained wave height results from the radar signal are shown in Fig. 11. The radar successfully detects the water level changes over the 15-min measurement period. While there are no direct comparison data available, the shape of the time history shows the characteristic surf bores followed by backwash and range of the measurements are consistent with those in the literature (e.g., Lanckriet et al. 2014). The baseline of the

FIG. 9. Continuous wave radar setup at Mickler Beach.

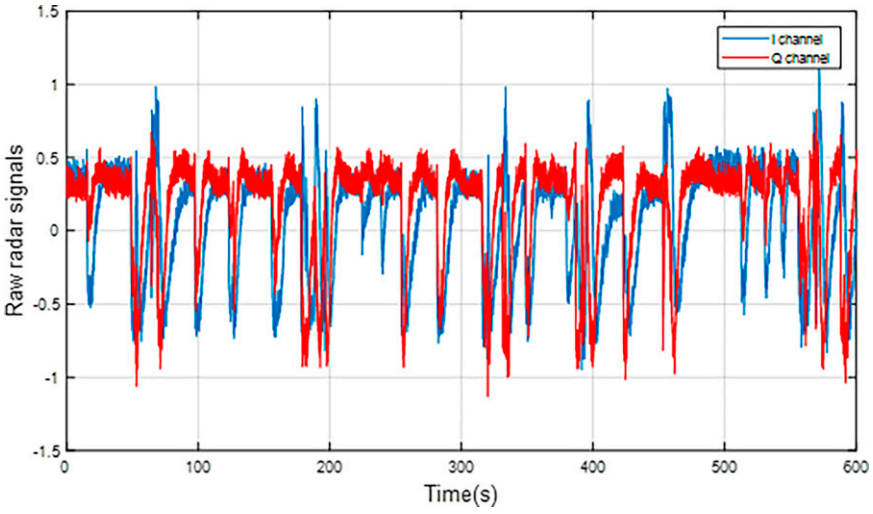


FIG. 10. Raw radar baseband signals during run-up tests.

distance measurement from the radar is increasing a small slope (less than 2%) due to sand accumulating around the support post during recording, thereby decreasing the distance between the radar and the target surface.

Additional run-up tests were conducted at Crescent Beach in St. Johns County, Florida, to validate the use of a multiradar network for spatial water level detection. Two first-generation radars operating in the interactive mode were used to conduct measurements. The radars took measurements simultaneously as a network and communicated wirelessly with single base station via XBee radio. The RF signals of each individual radar have different frequency offsets from the baseband frequency that distinguish the radar signals, so there is no interference between different radars operating simultaneously. Each radar was mounted to an aluminum plate with a cylinder column connecting the plate and the bottom of a tripod canopy. The radar was packed in a waterproof compact enclosure with the radar's antenna facing down to the sand surface and monitor wave run-up events. The radar's heights were 119 and 107 cm above the sand surface, respectively. The radar closer to the ocean was identified as radar A and the other one radar B. The distance between the two radars was ~660 cm. The tripods feet were fixed on the beach to avoid any potential vibrations or position changes of the sensor caused by wind or wave. The experimental setup and schematic are shown in Figs. 12 and 13.

The wave run-up measurements were captured with the two radars continuously for 15 min. Considering the small water level changes, arctangent demodulation was used for achieving water level measurement results. One segment

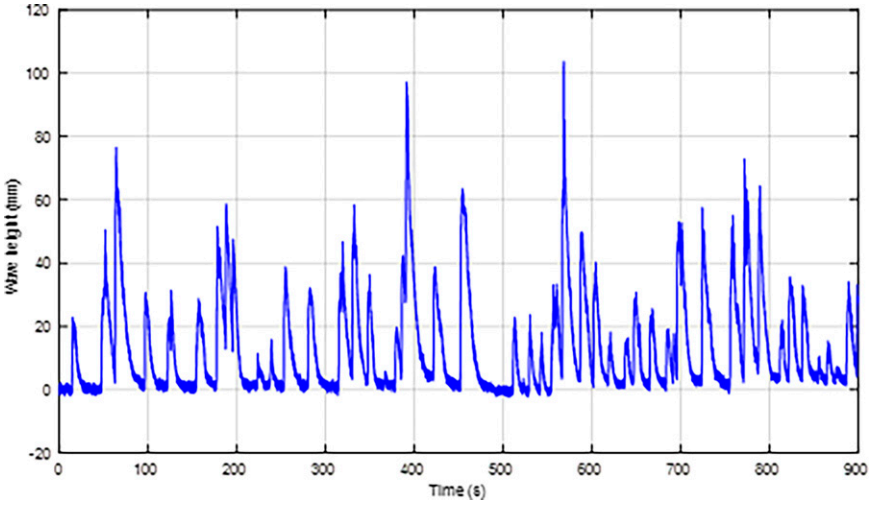


FIG. 11. Run-up measurement results from radar sensor.

FIG. 12. Crescent Beach experimental setup with two tripod-mounted, first-generation radars.

of the measurement data is shown in Fig. 14. Both radars successfully measured wave run-up events with radar A (closer to the ocean) capturing more waves and larger run-up depth than radar B, as expected. From the measurement results, the radars detected both the water level and datum (distance between the radar and sand surface) changes. The datum of the measurement changes during the measurements were believed to have been caused by the sand transport with the waves, albeit minimal. For future long-term monitoring, datum changes may be significant which must be considered. Also, during testing it was observed that some waves traveled in directions that were not normal to the shore, leading to the sensors measuring different waves. This experiment demonstrated the radar's capability of monitoring wave with the operation of two sensors simultaneously. With at least three radars, in theory, one could determine not only wave direction (using techniques common with three gauge pressure sensor arrays) but current magnitude and direction. Work on this subject is ongoing.

### c. *Flooding event in the Sparkill Creek*

The second-generation system with autonomous operation was deployed in the Sparkill Creek, a small tributary flowing into the Hudson River in Piermont. As part of a broader study regarding the risk of flooding in this region, the radar sensor, shown in Fig. 15, was deployed and operational from 25 October 2018 to 18 May 2019. The vertical position of the float switch for this deployment was placed slightly above mean higher high water (MHHW) level such that the system would only detect significant high water events. During this time, approximately 10 "events" were observed. As none of these events were significant and float switches were used to turn the sensors on/off, the amount of data recorded was only a few hours around the peak water level. A pressure sensor–based water level gauge was deployed with the radar for validation of the radar measurements. The pressure sensor also used a float switch (for both sensor battery conservation and to minimize biofouling of the pressure sensor) for activation but communicated with the base station computer via Wi-Fi to avoid interference with the 900 MHz XBee used by the radar. The radar sensor and a collocated pressure sensor were placed on a pier, approximately 15 m from a small boat house in which the mains-powered, base station computer system and modem were located. Locations of the radar sensor antenna and float switches for both sensors were surveyed such that all derived water levels could be referenced to the NAVD88 vertical datum. For further validation purposes, there was also a permanently deployed USGS gauge located at the end of the Piermont Pier approximately at the midpoint of the Hudson River. All of the radar $I/Q$ signals, pressure measurements, and their respective derived water levels for the 10 events collected in the Creek have been archived with the National Estuarine Reserve Research System (NERRS)

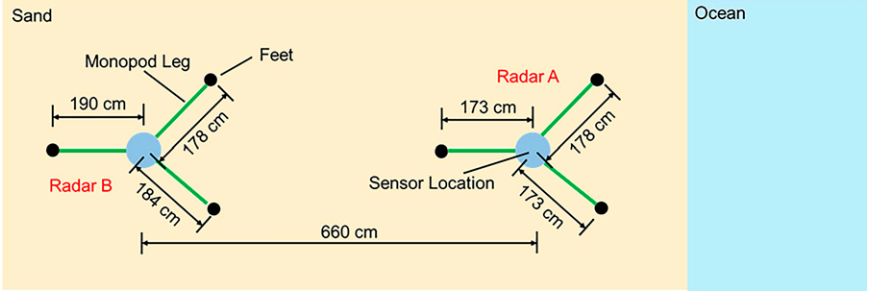


FIG. 13. Sensors' locations for Crescent Beach experiment.

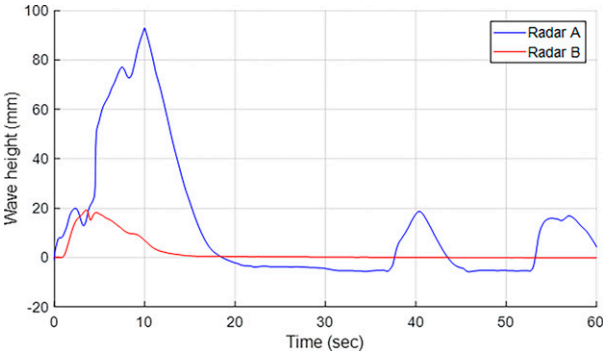


FIG. 14. Simultaneous run-up measurement results from two radar sensors for a 1-min interval.

Centralized Data Management Office and are accessible from the project page on the Science Collaborative website: (https://www.nerrssciencecollaborative.org/project/Sheng16).

For most of the events recorded (the larger ones), the $I/Q$ signals from the radars were able to be adequately demodulated and distance between the radar antenna and the water level accurately determined. Combining these distances with their surveyed vertical locations enabled the observation of water level with respect to the NAVD88 vertical datum. For these events, comparisons between the radar-derived water level and the collocated and nearby pressure sensor–based water level sensors compared well. An example of these comparisons for the high-water event that occurred on 25–27 November 2018 are shown in Fig. 16. The DACM approach was used for demodulation considering the large changes of water level and the ability to conduct demodulation in postprocessing after data were retrieved. RMS errors between radar sensor with USGS gauge for three different dates are 14.6, 14.9, and 9.8 mm, respectively. RMS errors between radar sensor and the pressure sensor–based water level gauge for three different dates are 18.3, 11.0, and 24.5 mm respectively. For the events in which the $I/Q$ signals did not demodulate cleanly, it is suspected that the relatively low power radar signal (and thus low SNR) was not able to adequately resolve the water surface interface, perhaps due to bubbles, debris, vegetation, etc. Work is ongoing on the enhancement of the demodulation algorithms.

## 5. Conclusions

The compact CW radar system has been tailored for both short- and long-term water level monitoring applications with two system generations and operating modes. The hardware design and embedded software program supports measurements of a range of water level fluctuation frequencies and amplitudes, with water level variations from centimeters to meters. The radar's water level measurement and communication performance has been validated in solitary wave detection laboratory experiments, swash zone free surface experiments, and flooding event monitoring. The radar system has demonstrated the potential to establish a multisensor network and a high level of water level detection accuracy. While this paper has demonstrated the radar's ability to measure a range of water elevation change conditions, efforts to classify hardware configurations (transmission power and antenna design) according to required

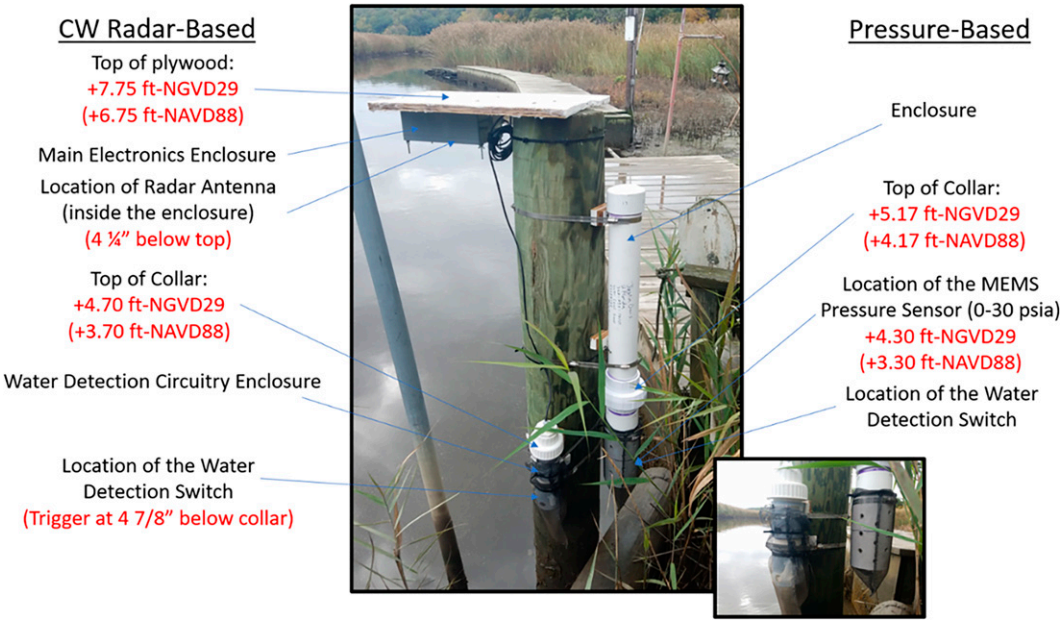


FIG. 15. Overview of the field-deployed continuous wave radar and pressure sensors deployed in the Sparkill Creek.

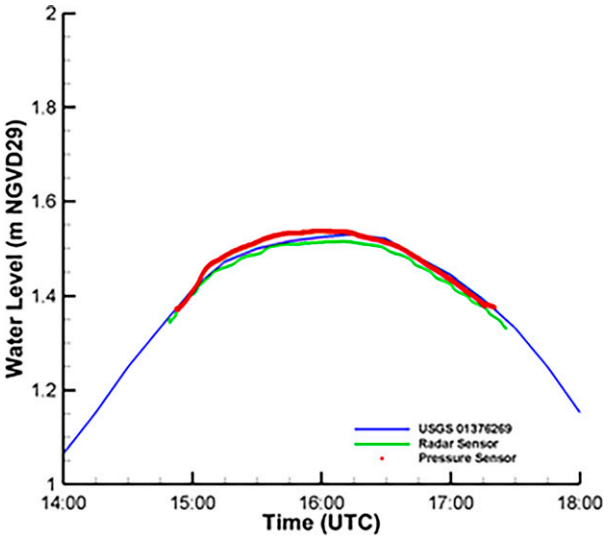


FIG. 16. (a) Comparison of continuous wave radar, collocated pressure sensor and a nearby USGS gauging station on 25 Nov 2018.

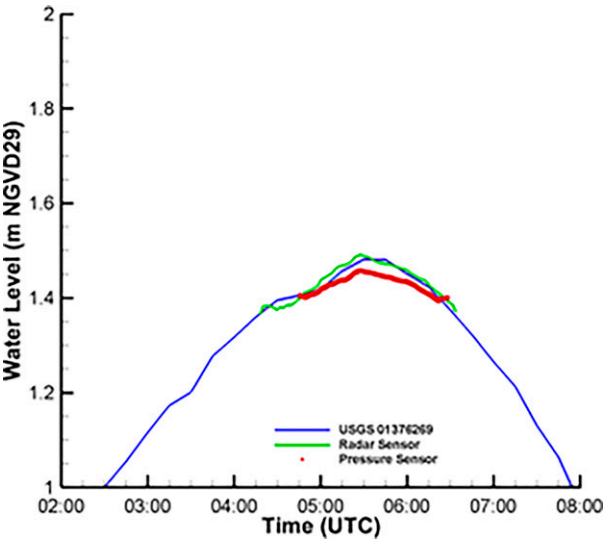


FIG. 16. (c) As in Fig. 16a, but for 27 Nov 2018.

measurement resolution and range are ongoing. As an example, one of the current limitations to the accuracy of the radar measurement is the relatively wide beamwidth (45°); a more focused beamwidth and higher signal power would enable accurate measurements at larger distances from the water surface (>2 m). In addition, surface disturbances such as bubbles and debris result in inaccurate measurements. Future work will assess hardware modifications to overcome this challenge. The use of multiple radars in a single location to measure wave directionality and surface current velocity is also under consideration.

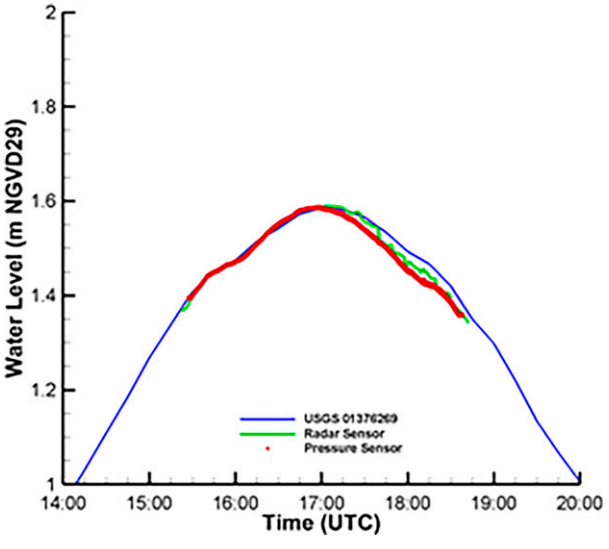


FIG. 16. (b) As in Fig. 16a, but for 26 Nov 2018.

*Acknowledgments.* The authors thank the National Science Foundation (Award 1452911) and the NOAA National Estuarine Reserve Research System (NERRS) Science Collaborative for their assistance in support of this research. The NERRS Science Collaborative supports collaborative research that addresses coastal management problems important to the reserves. The Science Collaborative is funded by the National Oceanic and Atmospheric Administration and managed by the University of Michigan Water Center (NAI4NOS4190145).

## REFERENCES

Anderson, A., D. Shirley, and L. Wilkins, 1972: An improved capacitive wavestaff for water surface wave measurements. *IEEE Int. Conf. on Engineering in the Ocean Environment*, Newport, RI, IEEE, 483–486, https://doi.org/10.1109/OCEANS.1972.1161158.

Aravamudhan, S., and S. Bhansali, 2008: Reinforced piezoresistive pressure sensor for ocean depth measurements. *Sens. Actuators*, **142A**, 111–117, https://doi.org/10.1016/j.sna.2007.04.036.

Arnaud, G., M. Mory, S. Abadie, and M. Cassen, 2009: Use of a resistive rods network to monitor bathymetric evolution in the surf/swash zone. *J. Coastal Res.*, **56**, 1781–1785.

Barjenbruch, U., S. Mai, N. Ohle, P. Mertinatis, and K. Irschik, 2002: Monitoring water level, waves and ice with radar gauges. *Proc. Hydro 2002 Conf.*, Kiel, Germany, Hydrographic Society, 328–337, https://www.lufi.uni-hannover.de/fileadmin/lufi/publications/60_radar_hydro.pdf.

Bera, S. C., J. K. Ray, and S. Chattopadhyay, 2006: A low-cost noncontact capacitance-type level transducer for a conducting liquid. *IEEE Trans. Instrum. Meas.*, **55**, 778–786, https://doi.org/10.1109/TIM.2006.873785.

Collard, F., F. Ardhuin, and B. Chapron, 2005: Extraction of coastal ocean wave fields from SAR images. *IEEE J. Oceanic Eng.*, **30**, 526–533, https://doi.org/10.1109/JOE.2005.857503.

Cui, J., R. Bachmayer, B. DeYoung, and W. Huang, 2018: Ocean wave measurement using short-range K-band narrow beam continuous wave radar. *Remote Sens.*, **10**, 1242, https://doi.org/10.3390/rs10081242.

——, ——, ——, and ——, 2019: Experimental investigation of ocean wave measurement using short-range K-band radar: Dock-based and boat-based wind wave measurements. *Remote Sens.*, **11**, 1607, https://doi.org/10.3390/rs11131607.

D'Asaro, E., and Coauthors, 2014: Quantifying upper ocean turbulence driven by surface waves. *Geophys. Res. Lett.*, **41**, 102–107, https://doi.org/10.1002/2013GL058193.

Farooqui, M. F., C. Claudel, and A. Shamim, 2014: An inkjet-printed buoyant 3-D Lagrangian sensor for real-time flood monitoring. *IEEE Trans. Antennas Propag.*, **62**, 3354–3359, https://doi.org/10.1109/TAP.2014.2309957.

Ferreira, L., P. Antunes, F. Domingues, P. Silva, and P. André, 2012: Monitoring of sea bed level changes in nearshore regions using fiber optic sensors. *Measurement*, **45**, 1527–1533, https://doi.org/10.1016/j.measurement.2012.02.026.

Fisher, D. K., and R. Sui, 2013: An inexpensive open-source ultrasonic sensing system for monitoring liquid levels. *CIGR J.*, **15**, 328–334.

Gesch, D. B., 2009: Analysis of lidar elevation data for improved identification and delineation of lands vulnerable to sea-level rise. *J. Coastal Res.*, **2009**, 49–58, https://doi.org/10.2112/SI53-006.1.

Goodman, L., and E. R. Levine, 1990: Vertical motion of neutrally buoyant floats. *J. Atmos. Oceanic Technol.*, **7**, 38–49, https://doi.org/10.1175/1520-0426(1990)007<0038:VMONBF>2.0.CO;2.

Grabemann, I., and R. Weisse, 2008: Climate change impact on extreme wave conditions in the North Sea: An ensemble study. *Ocean Dyn.*, **58**, 199–212, https://doi.org/10.1007/s10236-008-0141-x.

Gu, C., W. Xu, G. Wang, T. Inoue, J. A. Rice, L. Ran, and C. Li, 2014: Noncontact large-scale displacement tracking: Doppler radar for water level gauging. *IEEE Microwave Wireless Compon. Lett.*, **24**, 899–901, https://doi.org/10.1109/LMWC.2014.2352852.

Guan, S., J. A. Rice, C. Li, and C. Gu, 2014: Automated DC offset calibration strategy for structural health monitoring based on portable CW radar sensor. *IEEE Trans. Instrum. Meas.*, **63**, 3111–3118, https://doi.org/10.1109/TIM.2014.2317298.

——, ——, ——, Y. Li, and G. Wang, 2015: Dynamic and static structural displacement measurement using backscattering DC coupled radar. *Smart Struct. Syst.*, **16**, 521–535, https://doi.org/10.12989/sss.2015.16.3.521.

——, ——, ——, ——, and ——, 2017: Structural displacement measurements using DC coupled radar with active transponder. *Struct. Contr. Health Monit.*, **24**, e1909, https://doi.org/10.1002/stc.1909.

——, ——, ——, and N. J. DeMello, 2018: Smart radar sensor network for bridge displacement monitoring. *J. Bridge Eng.*, **23**, 04018102, https://doi.org/10.1061/(ASCE)BE.1943-5592.0001322.

Izaguirre, C., F. J. Méndez, M. Menéndez, and I. J. Losada, 2011: Global extreme wave height variability based on satellite data. *Geophys. Res. Lett.*, **38**, L10607, https://doi.org/10.1029/2011GL047302.

Jang, S., and Coauthors, 2010: Structural health monitoring of a cable-stayed bridge using smart sensor technology: Deployment and evaluation. *Smart Struct. Syst.*, **6**, 439–459.

Jeswin, C., B. Marimuthu, and K. Chithra, 2017: Ultrasonic water level indicator and controller using AVR microcontroller. *2017 Int. Conf. on Information Communication and Embedded Systems*, Chennai, India, IEEE, https://doi.org/10.1109/ICICES.2017.8070773.

Kelecy, T. M., G. H. Born, M. E. Parke, and C. Rocken, 1994: Precise mean sea level measurements using the global positioning system. *J. Geophys. Res.*, **99**, 7951–7959, https://doi.org/10.1029/93JC03355.

Kraus, N. C., A. Lohrmann, and R. Cabrera, 1994: New acoustic meter for measuring 3D laboratory flows. *J. Hydraul. Eng.*, **120**, 406–412, https://doi.org/10.1061/(ASCE)0733-9429(1994)120:3(406).

Krogstad, H. E., and S. F. Barstow, 1999: Satellite wave measurements for coastal engineering applications. *Coastal Eng.*, **37**, 283–307, https://doi.org/10.1016/S0378-3839(99)00030-7.

Lanckriet, T., J. A. Puleo, G. Masselink, I. L. Turner, D. Conley, C. Blenkinsopp, and P. Russell, 2014: Comprehensive field study of swash-zone processes. II: Sheet flow sediment concentrations during quasi-steady backwash. *J. Waterw. Port Coastal Ocean Eng.*, **140**, 29–42, https://doi.org/10.1061/(ASCE)WW.1943-5460.0000209.

Larson, K. M., J. S. Löfgren, and R. Haas, 2013: Coastal sea level measurements using a single geodetic GPS receiver. *Adv. Space Res.*, **51**, 1301–1310, https://doi.org/10.1016/j.asr.2012.04.017.

Li, C., and J. Lin, 2008: Random body movement cancellation in Doppler radar vital sign detection. *IEEE Trans. Microwave Theory Tech.*, **56**, 3143–3152, https://doi.org/10.1109/TMTT.2008.2007139.

——, V. M. Lubecke, O. Boric-Lubecke, and J. Lin, 2013: A review on recent advances in Doppler radar sensors for noncontact healthcare monitoring. *IEEE Trans. Microwave Theory Tech.*, **61**, 2046–2060, https://doi.org/10.1109/TMTT.2013.2256924.

Möller, I., and Coauthors, 2014: Wave attenuation over coastal salt marshes under storm surge conditions. *Nat. Geosci.*, **7**, 727–731, https://doi.org/10.1038/ngeo2251.

Nerem, R. S., D. P. Chambers, C. Choe, and G. T. Mitchum, 2010: Estimating mean sea level change from the TOPEX and Jason altimeter missions. *Mar. Geod.*, **33** (Suppl. 1), 435–446, https://doi.org/10.1080/01490419.2010.491031.

Oroza, C., A. Tinka, P. K. Wright, and A. M. Bayen, 2013: Design of a network of robotic Lagrangian sensors for shallow water environments with case studies for multiple applications. *Proc. Inst. Mech. Eng.*, **227C**, 2531–2548, https://doi.org/10.1177/0954406213475947.

Park, J., R. Heitsenrether, and W. Sweet, 2014: Water level and wave height estimates at NOAA tide stations from acoustic and microwave sensors. *J. Atmos. Oceanic Technol.*, **31**, 2294–2308, https://doi.org/10.1175/JTECH-D-14-00021.1.

Pieraccini, M., M. Fratini, F. Parrini, G. Macaluso, and C. Atzeni, 2004: High-speed CW step-frequency coherent radar for dynamic monitoring of civil engineering structures. *Electron. Lett.*, **40**, 907–908, https://doi.org/10.1049/el:20040549.

Pistrika, A. K., and S. N. Jonkman, 2010: Damage to residential buildings due to flooding of New Orleans after Hurricane Katrina. *Nat. Hazards*, **54**, 413–434, https://doi.org/10.1007/s11069-009-9476-y.

Poate, T., G. Masselink, M. Davidson, R. McCall, P. Russell, and I. Turner, 2013: High frequency in-situ field measurements of morphological response on a fine gravel beach during energetic wave conditions. *Mar. Geol.*, **342**, 1–13, https://doi.org/10.1016/j.margeo.2013.05.009.

Poulter, B., and P. N. Halpin, 2008: Raster modelling of coastal flooding from sea-level rise. *Int. J. Geogr. Inf. Sci.*, **22**, 167–182, https://doi.org/10.1080/13658810701371858.

Rorbaek, K., and H. Andersen, 2000: Evaluation of wave measurements with an acoustic Doppler current profiler. *OCEANS 2000 MTS/IEEE Conf.*, Providence, RI, IEEE, 1181–1187, https://doi.org/10.1109/OCEANS.2000.881761.

Theuerkauf, E. J., A. B. Rodriguez, S. R. Fegley, and R. A. Luettich Jr., 2014: Sea level anomalies exacerbate beach erosion. *Geophys. Res. Lett.*, **41**, 5139–5147, https://doi.org/10.1002/2014GL060544.

Turner, I. L., P. E. Russell, and T. Butt, 2008: Measurement of wave-by-wave bed-levels in the swash zone. *Coastal Eng.*, **55**, 1237–1242, https://doi.org/10.1016/j.coastaleng.2008.09.009.

Wahl, T., S. Jain, J. Bender, S. D. Meyers, and M. E. Luther, 2015: Increasing risk of compound flooding from storm surge and rainfall for major US cities. *Nat. Climate Change*, **5**, 1093–1097, https://doi.org/10.1038/nclimate2736.

Wang, J., X. Wang, L. Chen, J. Huangfu, C. Li, and L. Ran, 2014: Noncontact distance and amplitude-independent vibration measurement based on an extended DACM algorithm. *IEEE Trans. Instrum. Meas.*, **63**, 145–153, https://doi.org/10.1109/TIM.2013.2277530.

Warner, J. C., C. R. Sherwood, R. P. Signell, C. K. Harris, and H. G. Arango, 2008: Development of a three-dimensional, regional, coupled wave, current, and sediment-transport model. *Comput. Geosci.*, **34**, 1284–1306, https://doi.org/10.1016/j.cageo.2008.02.012.

Wöppelmann, G., B. M. Miguez, M.-N. Bouin, and Z. Altamimi, 2007: Geocentric sea-level trend estimates from GPS analyses at relevant tide gauges world-wide. *Global Planet. Change*, **57**, 396–406, https://doi.org/10.1016/j.gloplacha.2007.02.002.

Yang, Z., M. Li, and Y. Liu, 2007: Sea depth measurement with restricted floating sensors. *28th IEEE Int. Real-Time Systems Symp.*, Tucson, AZ, IEEE, 469–478, https://doi.org/10.1109/RTSS.2007.37.

Zhang, K., 2011: Analysis of non-linear inundation from sea-level rise using lidar data: A case study for south Florida. *Climatic Change*, **106**, 537–565, https://doi.org/10.1007/s10584-010-9987-2.